



Black phosphorus: A promising two dimensional visible and near-infrared-activated photocatalyst for hydrogen evolution

Mingshan Zhu, Yasuko Osakada, Sooyeon Kim, Mamoru Fujitsuka, Tetsuro Majima *

The Institute of Scientific and Industrial Research (SANKEN), Osaka University, Mihogaoka 8-1, Ibaraki, Osaka 567-0047, Japan



ARTICLE INFO

Article history:

Received 20 April 2017

Received in revised form 29 May 2017

Accepted 3 June 2017

Available online 4 June 2017

Keywords:

Black phosphorus

Two dimensional

Visible and near-infrared

Photocatalyst

Hydrogen evolution

ABSTRACT

The search for active photocatalysts that directly split water to hydrogen (H_2) under visible and near-infrared (NIR) light irradiation remains one of the most challenging tasks for solar energy utilization. Here we report that two dimensional (2D) black phosphorus (BP) nanoflakes can harness visible and NIR light for H_2 evolution. In the presence of reduced graphene oxide and Pt nanoparticles, ca. 5.13 and 1.26 μmol H_2 were obtained after excited BP nanoflakes under >420 nm and >780 nm irradiation for 4 h, respectively. The apparent quantum efficiencies (AQEs) were as high as approximately 8.7% at 420 ± 5 nm (visible) and 1.5% at 780 ± 5 nm (NIR), respectively. These results indicate that 2D BP can be used as visible- and NIR-activated elemental photocatalyst in artificial photosynthesis and renewable energy conversion.

© 2017 Elsevier B.V. All rights reserved.

1. Introduction

Solar energy, as a free, clean, green, and inexhaustible resource, has long been considered as one of the most promising renewable sources of energy [1–3]. The search for semiconductor photocatalysts in splitting the water to hydrogen (H_2) has attracted considerable attention since the first discovery of water splitting on a TiO_2 electrode under ultraviolet (UV) light irradiation in 1972 [3–8]. Up to now, great efforts have been made in developing diversified semiconductor photocatalysts for efficient splitting of water [4–6]. However, most of the traditional semiconductors such as TiO_2 have a wide bandgap (>3.2 eV), which means that UV light is necessary to activate their photocatalytic activities [4–6]. In our incoming solar spectrum, the UV light only accounts for 5%, while the visible light (~48%) and the near-infrared (NIR) light (~44%) account for more than 90% not to be utilized to activate the traditional semiconductor photocatalysts [4,9].

A great deal of time and efforts have been dedicated to achieve a novel photocatalyst that can harvest the broad range of solar light, especially in NIR region, over the past few decades. However, the search for such NIR-light-driven photocatalysts has focused mainly on photosensitization, upconversion materials, and a few of NIR photocatalysts, such as carbon quantum dots, $Cu_2(OH)PO_4$, and Bi_2WO_6/TiO_2 heterostructures [9–14]. Seriously, the above find-

ings bear either low photocatalytic efficiency based on narrow absorption or synthetic difficulty. To search for a photocatalyst with broadband solar absorption especially covering the NIR range still remains a formidable challenge.

Since the first report on field-effect transistors in 2014, ultrathin black phosphorus (BP), as a new two dimensional (2D) material, grabs a big triumph in electronics, optoelectronics, and sensors, and becomes a rapidly rising star in material science [15–21]. As one of the most infusive properties, the direct bandgap of BP can be tuned sufficiently for photon absorption in the UV and visible region, and also NIR region [21–25], indicating that BP is suitable to be an efficient photocatalyst with broadband solar absorption [25–31]. Recently, Sa et al. [26] demonstrated the potential of BP as a water splitting photocatalyst for H_2 evolution based on density functional theory calculations. Qiao's group [27] had critically reviewed the fundamental electronic, optical and chemical properties of BP and also assessed its suitability and stability as a future water splitting photocatalyst.

Here we demonstrate 2D BP nanoflakes can be worked as a broad spectrum photocatalyst, which can harness visible and NIR light for photocatalytic H_2 evolution. In the presence of reduced graphene oxide (RGO) and Pt nanoparticles, the optimum H_2 evolution activities are ca. 5.13 and 1.26 μmol with rate of 3.4 and $0.84 \text{ mmol g}^{-1} \text{ h}^{-1}$ under >420 nm and >780 nm irradiation, respectively. The efficient electrons transfer from excited BP nanoflakes and Pt/RGO contribute to NIR light driven photocatalytic H_2 evolution, which was proved by photoelectrochemical measurements and transient absorption. Our findings render 2D BP to be a broad

* Corresponding author.

E-mail address: majima@sanken.osaka-u.ac.jp (T. Majima).

spectrum photofunctional material and grab an attractive potential application in solar energy conversion.

2. Results and discussion

The ultrathin BP nanoflakes were prepared by using a basic N-methyl-2-pyrrolidone (NMP) solvent exfoliation method [32]. To directly visualize the effect of the above ultrasonication exfoliation, the scanning electron microscopy (SEM) images of the original BP powders (Fig. S1a) and the sediments separated after centrifugation (Fig. S1b) were examined. The results show that the raw BP powder consists of bulky plates, while the sediments separated after ultrasonication and centrifugation have much thinner and layers structures. It is suggested that the ultrasonication exfoliates the bulk BP to give BP nanoflakes. After centrifugation, a brownish dispersion was obtained, resulting in BP nanoflakes NMP dispersion (Fig. S2).

To explore the fine morphology and crystallinity of as-exfoliated BP, the above suspension was investigated by means of atomic force microscopy (AFM) and transmission electron microscopy (TEM). The thickness of BP nanoflakes ranging from 2.4 to 5.2 nm was measured by AFM to be close to that of the 4–10 phosphorus atomic layers (Figs. S3 and S4) based on the monolayer thickness of 0.5–0.7 nm [20]. Moreover, ultrathin sheet-like structures with the size of 200 nm ~ 2 μm of BP nanoflakes were revealed from TEM images on randomly place of carbon-coated copper grid, which is used to hold samples (Fig. 1a and Fig. S5). The crystallinity of the as-prepared BP nanoflakes was studied by high-resolution TEM (HRTEM) (Fig. 1b) and selected-area electron diffraction (SAED) (Fig. 1c). Firstly, clear lattice fringes were observed from BP layers and those of 2.18 Å and 1.65 Å correspond to the x and z directions, respectively [25]. The SAED image suggests the as-prepared BP nanoflakes to be single crystalline with [010] preferential orientation [25], which is consistent with BP lattice parameters. The uniform lattices (Fig. 1b and c) suggest that the nanoflakes produced by solvent-exfoliation retain the original crystalline state.

Raman spectroscopy is an effective technique for the identification of crystallographic orientation and chemical composition of materials. Herein, Raman spectra were measured to study the structural transformation of BP after liquid exfoliation process (Fig. S6). Bulk BP exhibits characteristic peaks at 362.3, 438.7, 466 cm⁻¹, which assigned to A_g¹, B_{2g}, and A_g² phonon modes of vibration originating from in-plane (B_{2g} and A_g²) and out-of-plane (A_g¹) vibrational modes, respectively [25,32]. On the other hand, these peaks for BP nanoflakes slightly shift to 363.7, 439.4, and 466.7 cm⁻¹, respectively, compared to bulk BP. The similar shifts have been found in the previous reports [25], indicating the successful exfoliation process.

The quality of BP nanoflakes was further analyzed by performing energy-dispersive X-ray spectroscopy (EDX) with the spectra on the SEM and mapping on the HAADF-STEM (Figs. S7 and S8), respectively. Firstly, the as-exfoliated sample showed C, O, and P elements clearly (Fig. S7a). The C and O signals were coming from the carbon gel substrate, which was used for supporting samples during the measurements. Compared with blank comparison, only small amount of P was oxidized after as-exfoliated BP samples were stored for one month. Furthermore, the HAADF-STEM image and corresponding EDX elemental mapping of P, C, and O were detected (Fig. S8). The elemental mapping for phosphorus extracted from the spectrum image confirms that the phosphorus signal is strongly correlated with the nanoflake location and other elements detected are those associated with the TEM grid, suggesting that the nanoflakes produced are consistent with their crystalline nature.

X-ray photoelectron spectroscopy (XPS) spectra of bulk BP and BP nanoflakes were measured (Fig. S9) to further confirm the quality of as-prepared BP nanoflakes. Firstly, in the full spectra of bulk BP and BP nanoflakes, there were some contaminant elements observed beside P element. These contaminant elements are probably originated from environment atmospheres. The control experiment for carbon gel was carried out to show same elements for bulk BP and BP nanoflakes except the P element. The high resolution XPS spectra of P 2p in bulk BP and BP nanoflakes display two bands at ca. 129.7 and 130.5 eV, corresponding to P 2p_{3/2} and P 2p_{1/2} binding energies, respectively. Besides, a sub-band is apparent at 134.1 eV, corresponding to oxidized phosphorus (i.e., P_xO_y) [20]. The ratio of oxidized phosphorus (P_xO_y) in BP nanoflakes is higher than that in bulk BP, suggesting that the surface of BP nanoflakes was slightly oxidized after exfoliation process. Furthermore, the O 1s peaks of bulk BP and BP nanoflakes were deconvoluted into peaks for O=C=O (530.6 eV), oxygen (531.6 eV), C=O (532.2 eV), C—OH/C—O—C (532.8 eV), H₂O (533.3 eV), and P—O_x (534.1 eV) [33]. The ratio of P—O_x in BP nanoflakes is also higher than that in bulk BP, further showing the slight oxidation of as-synthesized BP nanoflakes.

As the most infusive properties, the broadband solar absorption of BP nanoflakes makes them to be used as an effective visible and NIR optical material [21–24,30]. To observe the broadband solar absorption property of the as-exfoliated BP nanoflakes, the UV-vis-NIR spectra of different concentration BP aqueous dispersions and the corresponding photograph were shown in Fig. S10. The sample displays a brownish color and a very broad absorption from UV to NIR region. This intrinsic feature indicates that as-prepared BP nanoflakes might have potential application possibilities as visible and NIR light-induced photocatalysts.

The photocatalytic H₂ evolution reactions were performed over BP nanoflakes as photocatalyst under visible and NIR light irradiation with ethylenediaminetetraacetic acid (EDTA) as a sacrificial agent. No H₂ evolution was observed when only bare BP nanoflakes were used in the reaction under light irradiation. Generally, an efficient photocatalytic H₂ evolution system usually consists of a sacrificial agent, photosensitizer, electron mediator, and cocatalyst [34,35]. As known, the most efficient H₂ evolution catalyst is Pt nanoparticles, because Pt has a low overpotential for proton reduction to evolve H₂ [34,35]. However, when we mixed the commercial Pt colloids with BP, trace amount of H₂ was observed. This is probably due to poor electron transfer efficiency between BP and Pt nanoparticles without an electron mediator.

Recently, 2D RGO has been confirmed as an excellent electron mediator for storing and shuttling electrons [36,37]. Accordingly, the Pt/RGO nanocomposites were introduced to the above reaction, where RGO served as an electron mediator and Pt nanoparticles worked as a co-catalyst. The morphology of as-prepared Pt/RGO nanocomposite was studied by TEM. As shown in Fig. 2a, the Pt nanoparticles with the average size of 4.2 ± 0.5 nm were uniformly distributed on the wrinkled RGO surface. Furthermore, the ternary BP/Pt/RGO nanocomposite was obtained via mixing the as-prepared Pt/RGO and BP nanoflakes under the ultrasonic process. Fig. 2b clearly shows that the sheet-like Pt/RGO nanostructures were assembled on the surface of 2D BP nanoflakes. To further confirm the formation of the hybridization of BP and Pt/RGO, the HRTEM and EDX mapping on the HAADF-STEM of ternary BP/Pt/RGO nanocomposite. Fig. 2c shows that the evident lattice fringes indicating a lattice spacing of ca. 0.227 nm and 0.218 nm, which correspond to the (111) facets of Pt and (020) planes of BP, respectively, could be easily observed in the representative HRTEM images. Meanwhile, the lattice fringes of graphene also easily observed from the HRTEM image. The HAADF-STEM image and corresponding EDX elemental mapping of P and Pt (Fig. 2d–f) clearly show the different element distributed on the surface of the

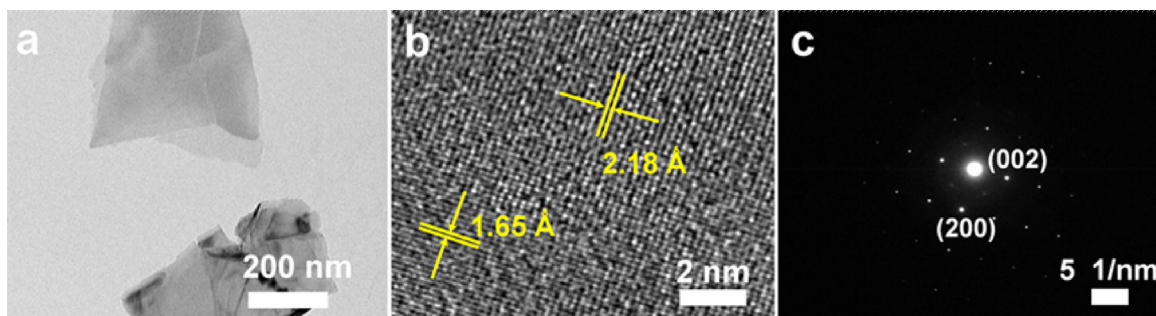


Fig. 1. TEM (a) and HRTEM (b) images, and SAED pattern (c) of as-exfoliated BP nanoflakes.

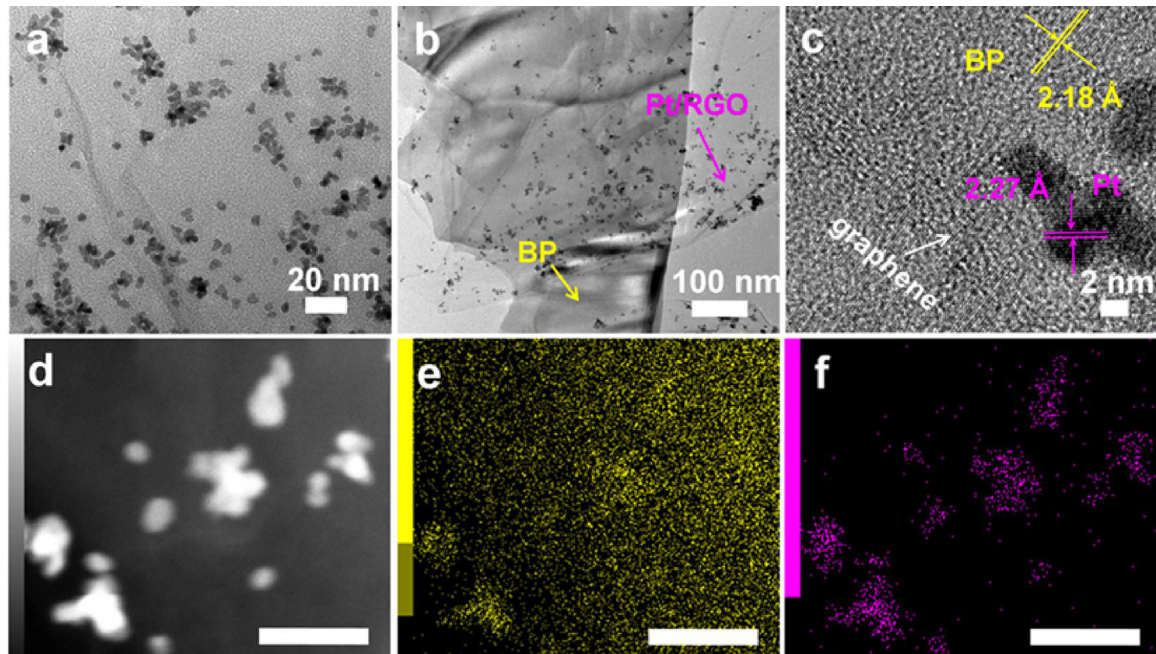


Fig. 2. TEM images of Pt/RGO (a) and BP/Pt/RGO (b) composites. HRTEM (c), HAADF-STEM (d) images, and EDX elemental mapping of P (e) and Pt (f) in the cross section of BP/Pt/RGO. The scale bars in the panels of d–f are 20 nm.

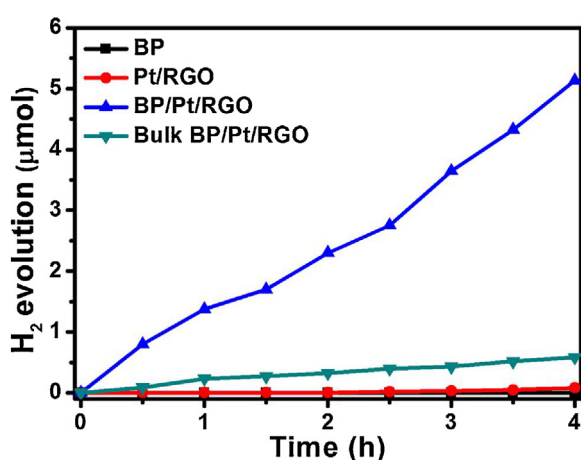


Fig. 3. Photocatalytic H₂ evolution of different samples under >420 nm irradiation by using water containing EDTA (0.02 M), BP (0.2 mg), RGO (0.1 mg), and Pt (75 μg).

ternary BP/Pt/RGO sheets. The UV-vis-NIR and Raman spectra of Pt/RGO refer to Fig. S11.

As expected, in the presence of Pt/RGO and EDTA, the amount of H₂ generated from the system increased with time (Fig. 3).

reached approximately 5.13 μmol under >420 nm irradiation for 4 h. Methanol and triethanolamine (TEOA) were also used as the sacrificial reagent (Fig. S12), in which similar phenomena were observed. As a reference experiment, only 0.08 μmol was detected under the similar condition using only Pt/RGO without BP nanoflakes. This result indicates that BP nanoflakes play a crucial role in the photocatalytic H₂ evolution. Compared to bulk BP (0.52 μmol), BP nanoflakes exhibited superior H₂-evolution activity. This higher activity is probably attributed to the higher surface area and the lower electron–hole-recombination rate in ultrathin 2D materials [38].

The influence of the amount of Pt/RGO loading on H₂ evolution was further investigated. The optimal amount of Pt/RGO in the present photocatalytic system was demonstrated to be 75 μg Pt loading, which led to a H₂ evolution rate of 3.4 mmol g⁻¹ h⁻¹ (Fig. 4a). A further increase in the amount of Pt/RGO loading led to a decrease in activity, probably resulting from a decrease of light absorption owing to the formation of black Pt/RGO colloid. On the other hand, the effect on photocatalyst dose was also investigated. As shown in Fig. 4b, there is continuous enhancement in the hydrogen evolution rate with the increase in the photocatalyst dose. However, when the high concentrated dispersion was used, the increase of photocatalytic activity did not show liner

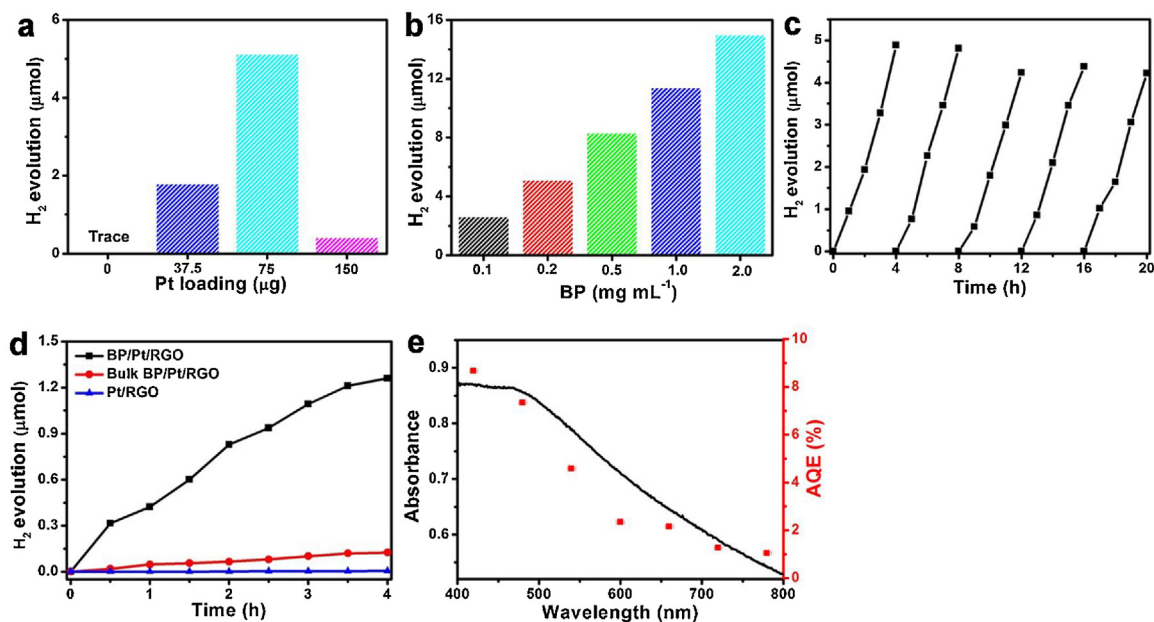


Fig. 4. Effect of Pt loading amounts (a) and BP concentration (b) in BP/Pt/RGO nanocomposites on photocatalytic H₂ evolution under >420 nm irradiation for 4 h. In (a) the ratio of Pt/RGO is unchanged. Cycle stability test on BP/Pt/RGO photocatalytic H₂ evolution (c). Photocatalytic H₂ evolution on different samples under >780 nm light irradiation (d). Wavelength-dependent AQE of photocatalytic H₂ evolution for 1 h using BP/Pt/RGO containing EDTA (0.02 M), BP (1.0 mg), RGO (0.5 mg), and Pt (0.38 mg) (e).

increase. This is because of the opaque dispersion in high concentrated dispersion block the utilization of incident light.

The photocatalytic stability of BP/Pt/RGO system was investigated by cyclic photocatalytic H₂ evolution experiments. Before the light irradiation was re-started, the catalytic system was treated by the ultrasonication for 10 min. As shown in Fig. 4c, continuous H₂ evolution was observed with no noticeable degradation in the subsequent runs, indicating BP nanoflake worked as a stable photocatalyst for H₂ evolution. The slight decrease of the activity during the recycling reactions might be attributed to loss of catalysts during centrifugation process, slight degradation of BP, and decrease in the concentration of sacrificial electron donor with long time irradiation. The stability of BP under different atmospheres and light irradiation was examined (Figs. S13–S15). Moreover, XPS, Raman, and TEM images of BP/Pt/RGO were measured before and after photocatalytic reaction to show no obvious change (Figs. S16–18), indicating that BP/Pt/RGO can be kept stable during photocatalytic reaction under visible-NIR light irradiation.

As the solar absorption of BP nanoflakes can be tuned sufficiently in the UV, visible, and NIR light region, showing BP is suitable for an activated photocatalyst under both visible and NIR light irradiation. To excite BP under NIR light irradiation for photocatalytic H₂ evolution, a xenon lamp with a 780 nm long-pass filter putting in front of the reactor and a 808 nm NIR laser were used as light source, respectively. Fig. 4d and Fig. S19 clearly show the continuous H₂ evolution was observed in BP/Pt/RGO system in the presence of EDTA as sacrificial reagents under >780 nm and 808 nm laser light irradiation. Approximately 1.26 and 0.88 μmol H₂ were obtained under >780 nm and 808 nm laser light irradiation for 4 h, with the H₂ evolution rate of 0.84 and 0.59 mmol g⁻¹ h⁻¹, respectively. As comparisons, the bulk BP/Pt/RGO exhibited relatively inferior H₂ evolution activity, while no H₂ evolution was observed for using Pt/RGO under >780 nm irradiation condition. These results evidently confirm that BP acts as a NIR-activated photocatalyst for splitting water to H₂.

To evaluate as-prepared samples as photocatalysts for solar energy conversion, the photocatalytic H₂ evolution activity of BP/Pt/RGO was measured under simulated solar (1 sun at AM

1.5G, ~100 mW cm⁻²) irradiation. Approximately 12.6 μmol H₂ was obtained under simulated solar light irradiation (Fig. S20). The wavelength dependent apparent quantum efficiency (AQE) of H₂ evolution over BP nanoflakes was shown to distinguish that the activity was driven by the light-excited electrons in BP nanoflakes under the optimal conditions. Fig. 4e shows that the action spectra of AQE of samples, wherein the AQE reached to 8.7% at 420 ± 5 nm and 1.5% at 780 ± 5 nm. The AQY decreased as the wavelength of the monochromatic light increased, and it quite well tracked the characteristic absorption of the BP. These results indicate that as-prepared BP nanoflakes can be applied for solar light-induced photocatalysts owing to their broad absorption property.

To demonstrate the BP nanoflakes can be used as photocatalysts and eliminate the effect of RGO, the photoreduction of Ag under >420 nm and 808 nm laser irradiation were studied by using BP and RGO. 0.1 mg corresponding samples (BP or RGO nanosheets) was added into 4 mL AgNO₃ (0.01 M) aqueous solution and then deaerated by Ar bubbling for 30 min. After that, the reactor was irradiated with >420 light or 808 nm laser light (light intensity was ca. 100 mW) for 1 h. After reaction, the sediments were collected by centrifugation and washed thoroughly with water. In order to confirm the formation of Ag nanoparticles, we characterized the above sediments by TEM. As shown in Fig. 5, there were lots of irregular particles on the surface of BP nanosheets both under >420 and 808 nm laser light irradiation. However, when the bare RGO nanosheets were used, only several Ag particles were observed on the surface RGO nanosheets. This result suggested that the BP nanoflakes can be served as efficient photocatalyst for the reduction of Ag ions under visible and NIR light irradiation, but RGO nanosheets do not under the present conditions.

It is well known that the graphene acted as ideal energy and/or electron acceptor with hybridization of semiconductors. Firstly, to show the interfacial electron transfer between BP and RGO nanosheets, the J–V curves (photocurrent density vs. the applied potential) and electrochemical impedance spectroscopy (EIS) under dark and light irradiation of BP/RGO composites were investigated. As shown in Fig. 6a, the photocurrent densities of electrodes under dark sharply increased when the electrodes were

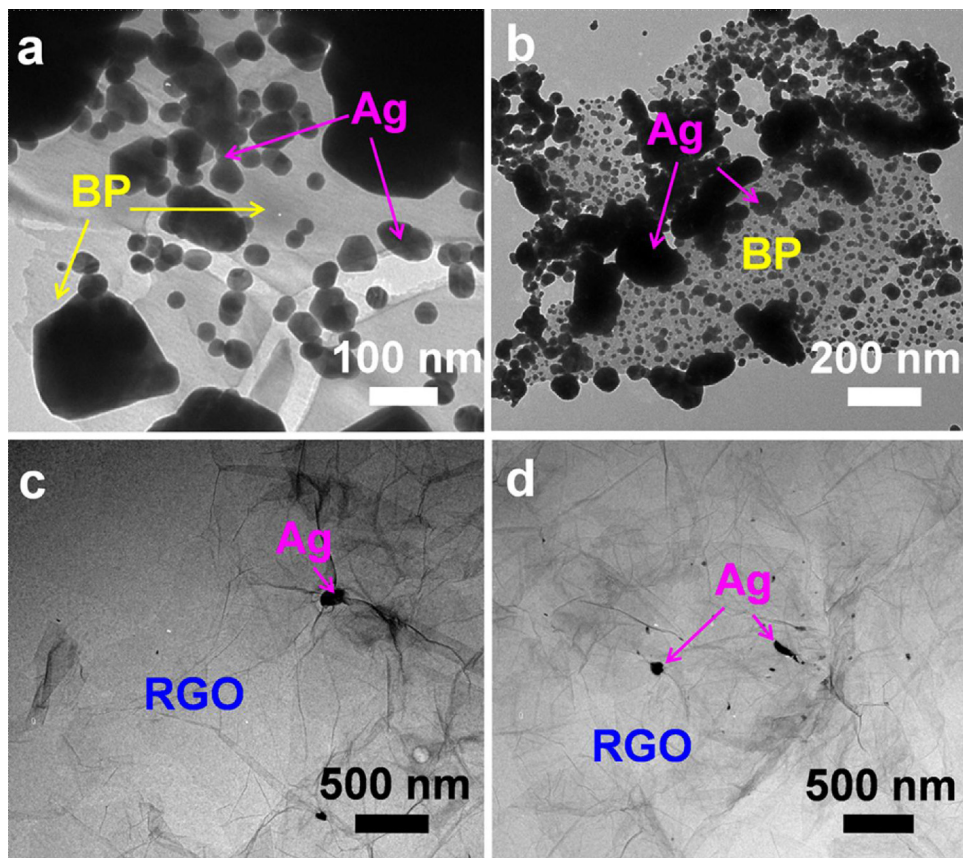


Fig. 5. TEM images of Ag/BP nanoflakes (a and b) and Ag/RGO nanosheets (c and d) by using >420 nm (a, and c) and 808 nm laser (b and d) light irradiation.

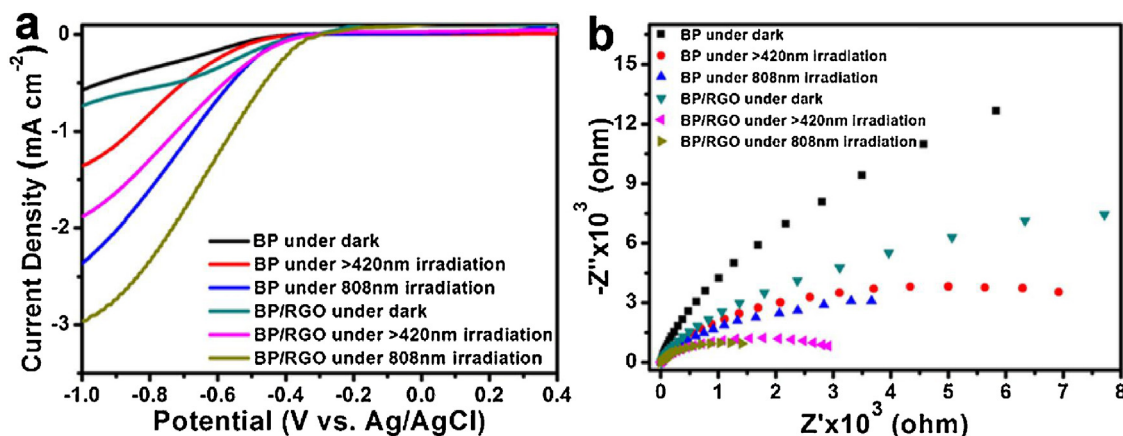


Fig. 6. J-V curves plotting the photocurrent density as a function of the applied potential (a). EIS spectra of different samples in 0.1 M NaOH ethanol solution (b).

under >420 or 808 nm NIR light irradiation. This result means that when BP modified electrodes were under light irradiation, photons absorbed by BP generate electrons, producing higher photocurrent densities. After hybridization of RGO nanosheets, the photocurrent densities of BP/RGO modified electrodes showed a clear increase compared to bare BP, suggesting that the RGO nanosheets can enhance electron transport from BP to electrode.

In addition, EIS spectra were measured to verify the internal resistances and interfacial electron transfers of samples under dark, and under >420 or 808 nm NIR light irradiation, in which the smaller semicircle arc in the EIS spectra indicates faster interfacial electron transfer [39,40]. The diameter of the semicircle arc of the BP/RGO

modified electrode was smaller than that of only BP modified electrode (Fig. 6b), suggesting the efficient interfacial electron transfer in BP/RGO. Furthermore, under light (>420 or 808 nm laser) irradiation, the corresponding diameter of semicircle arc was much smaller than that for no light irradiation, confirming that light irradiation promotes the electrons mobility at the surface of electrode.

Although the above PEC measurements can provide information on charge transfer, direct measurement of charge dynamics in photocatalysts is crucial for understanding the photocatalytic reaction mechanism. The transient absorption (TA) measurements of samples during femtosecond laser flash photolysis using 400 nm and 780 nm laser excitation were carried out (Fig. 7 and Fig. S21).

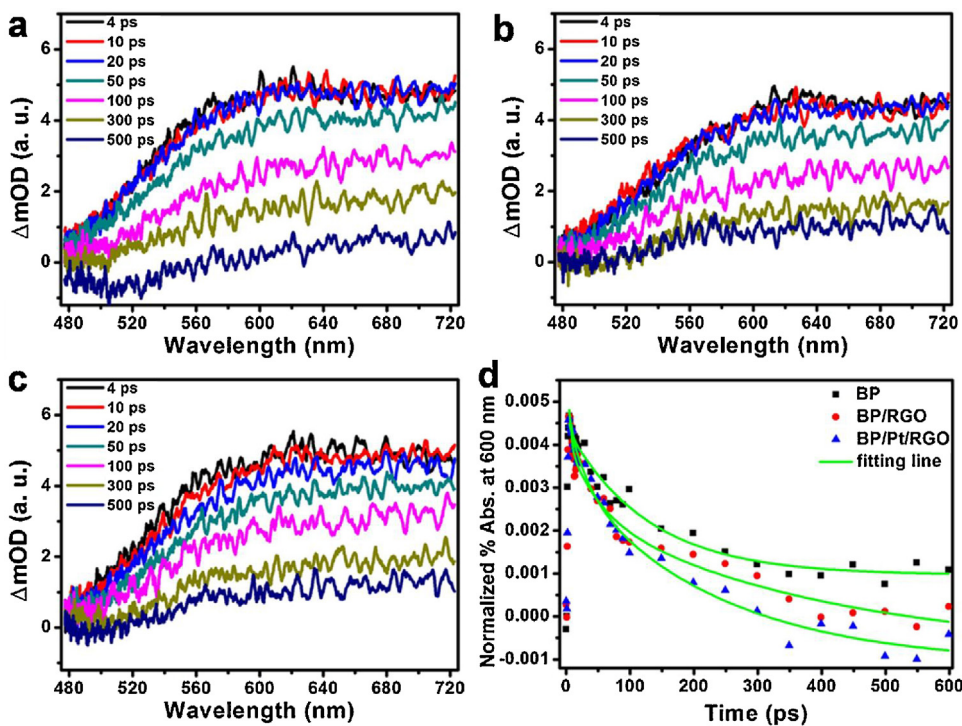


Fig. 7. Transient absorption spectra of BP (a), BP/RGO (b) and BP/Pt/RGO (c) under 400 nm excitation. Normalized transient absorption traces observed at 600 nm for the samples (d).

Firstly, after 400 nm excitation of BP-based samples, broad TA spectra appeared in the visible wavelength region. In a time period of 4–500 ps, the concentration of chargers decreased in a multi-exponential fashion owing to the charge recombination. After hybridization of RGO and Pt/RGO with BP, TA spectra were observed to be similar to that of pure BP. No detectable TA of RGO radical anion ($RGO^{•-}$) was observed in the wavelength region examined for both composites. This is owing to the small molar absorption coefficient of $RGO^{•-}$ and our detection limit in the wavelength region ($\Delta OD \sim 0.001$). When the samples were excited at 780 nm, the similar TA spectra were observed (Fig. S21). The result indicates that BP nanoflakes can be excited to give electron-hole pairs under visible and NIR light irradiation.

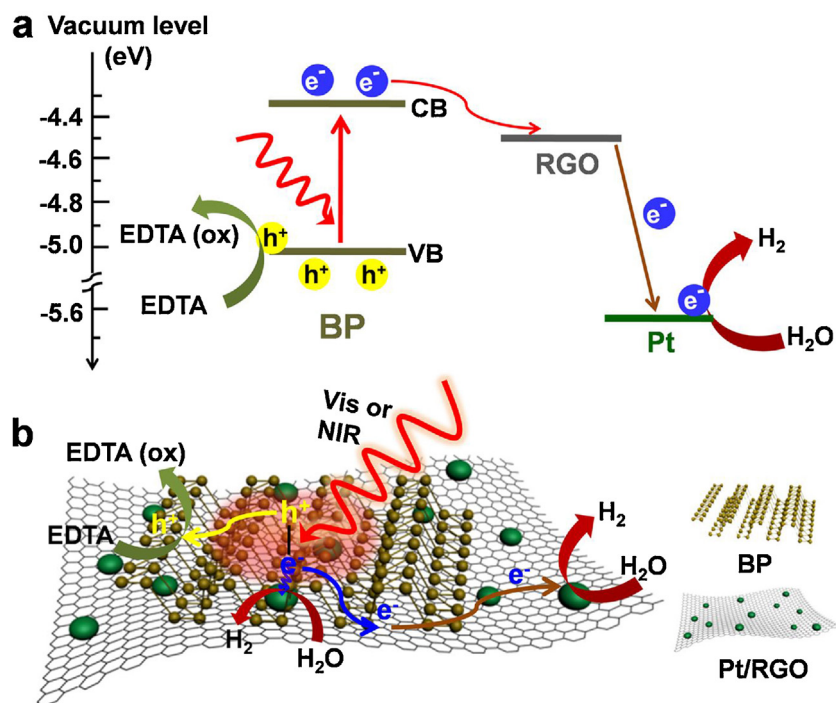
To evaluate the decay kinetics, the time profiles of absorption were fitted using two-exponential functions, and their lifetimes were summarized in Table S1. Firstly, it can be seen that although the BP/RGO and BP/Pt/RGO samples showed broad absorption spectra similar to pure BP, the decay kinetics are obviously different. The average decay lifetimes measured for pure BP were 226.3 for 400 nm excitation. After modifying BP by RGO or Pt/RGO, the decay lifetimes were found to decrease largely to 129.1 ps and 108.0 ps, respectively, under 400 nm light excitation. Similar tendency was observed under 780 nm excitation (Table S1). Such a decreased lifetime is well understood as arising from the opening of an additional channel of interfacial electron transfer from excited BP to RGO and the decorated metal nanoparticles [41–44]. For examples, Furube et al. discovered that the lifetime of TiO_2 was decrease with increasing of weight ration of Pt nanoparticles, indicating an electron migration from photoexcited TiO_2 to loaded Pt nanoparticles [42]. Similar phenomena were also observed in other hybrids system, such as CdSe/TiO₂ [43], CdSe/Pt or CdSe/Au [44].

Based on the above results, 2D BP nanoflakes were evidently demonstrated to be effective visible/NIR light activated photocatalysts for H_2 evolution. The possible mechanism for H_2 evolution of this system is illustrated in Scheme 1. Firstly, based on UV-visible

diffuse reflectance spectra modified by Kubelka–Munk function and Mott–Schottky plots (Fig. S22), the conduction band (CB) and valence band (VB) of BP nanoflakes were ca. -0.14 V and 0.52 V vs. NHE (4.36 eV and 5.06 eV vs. vacuum level), respectively. The CB level is suitable for H_2 generation when BP is photoexcited. Secondly, the excited BP nanoflakes will generate electrons and holes in CB and VB, respectively. The CB electrons are efficiently injected from the excited BP into RGO sheets to be trapped by Pt nanoparticles loaded on RGO. At the same time, the VB holes transport to BP nanoflakes to be captured by EDTA as a sacrificial electron donor. After trapped hole, the sacrificial agent of EDTA would be oxidized to intermediates such as formic acid, amines, aldehydes and carboxylic acids, etc. and finally decomposing into NH_3 and CO_2 [45,46]. Such effective charge transport in BP/Pt/RGO results in an efficient charge separation (CS). After enough electrons are trapped by Pt nanoparticles, the reduction of H^+ (water) occurs to generate H_2 .

3. Conclusions

In conclusions, we showed 2D BP nanoflakes with broad spectrum photocatalytic properties, which worked as visible and NIR activated photocatalysts for photocatalytic H_2 evolution. The optimum H_2 evolution reached to 5.13 and $1.26 \mu\text{mol}$ under >420 nm and >780 nm light irradiation, respectively, in the presence of Pt/RGO and EDTA. By combining photoelectrochemical measurements and transient absorption, we found efficiently charger transfer between excited BP nanoflakes and Pt/RGO, which contribute to the evolution of H_2 under visible and NIR light irradiation. We believe that these advances will render 2D BP to be a photo-functional material in solar energy conversion and open up a new avenue for the development of vis-NIR-light-driven photocatalysts for water splitting.



Scheme 1. Proposed schematic diagram (a) and reaction mechanism (b) for the visible and NIR light activated photocatalytic H₂ evolution of 2D BP nanoflakes and Pt/RGO.

4. Experimental section

4.1. Preparation of ultrathin BP nanoflakes

The ultrathin BP nanoflakes were prepared by using a basic NMP solvent exfoliation method [32]. The bulk BP crystals were purchased from Nanjing XFNANO Materials Tech Co., Ltd. (XF161, purity >99.998%). Bulk BP (20 mg) was lightly ground with pestle and mortar and immersed into 20 mL saturated NaOH/NMP. The dispersion was sonicated for 4 h with a tip sonicator (Misonix XL-2000) at 10 W output power under ice cooling. After exfoliation, the dispersion was centrifuged at 2000 rpm for 20 min with two times to remove nonexfoliated bulk BP. The supernatant was further centrifuged at 11000 rpm for 20 min to separate the ultrathin BP nanoflakes from the supernatant. After that, the precipitations were washing repeatedly with water and redispersed in 10 mL ultrapure Milli-Q water with ultrasonic process, resulting in ultrathin BP nanoflakes aqueous dispersion (0.2 mg mL⁻¹).

4.2. Preparation and characterization of BP/Pt/RGO nanocomposites

The Pt/RGO nanocomposites were synthesized by using an ethanol reduction method [47]. 2.5 mL graphene oxide aqueous dispersion (GO, 2 mg mL⁻¹, Sigma Aldrich) and 10 mL H₂PtCl₆·6H₂O aqueous solution (1 mg mL⁻¹, Sigma-Aldrich) were added into 12.5 mL ethanol solution. The pH of the mixture was adjusted to 10 with the aid of 0.1 M NaOH aqueous solution. Afterwards, the mixture was refluxed in an oil bath at 100 °C for 2 h under constant stirring. Finally, the sample was collected through high-speed centrifugation and thoroughly rinsing with methanol for three times. The precipitations were redispersed in 50 mL methanol with ultrasonic process (30 min), resulting in Pt/RGO nanocomposites.

The ternary BP/Pt/RGO nanocomposite was obtained via mixing different ratio of the as-prepared BP nanoflakes and Pt/RGO under the ultrasonication for 30 min.

4.2. Structural characterizations

The samples were characterized using SEM and EDX (JEOL, JSM-6330FT), TEM (JEOL, 2100, operated at 100 KV), HRTEM and HAADF-STEM-EDX (JEM-3000F, operated at 300 KV). The AFM images, without any image processing, were recorded on a SPI3800/SPA400 AFM (Seiko Inc., Tokyo, Japan) in tapping mode. The samples for AFM measurements were prepared by spraying a diluted suspension of the sample on a freshly cleaved mica surface and then dried in air. Absorption spectra were taken using quartz cuvettes of 1-cm path length on a Shimadzu UV-3600 UV-VIS-NIR spectrophotometer. UV-vis diffuse reflectance spectra were obtained on a JASCO V-770 UV-vis/NIR spectrophotometer. The Raman spectra were recorded on a Raman microscope (NR-1800, JASCO) using a 514.5-nm argon ion laser. X-ray photo-electron spectroscopy (XPS) was measured on a JEOL JPS-9010 MC spectrometer. The photoelectrochemical measurements were performed in beaker by using an electrochemical workstation (ALS, 660B) in a standard three electrode configuration with Pt wire, Ag/AgCl, and the modified GC electrode as the counter, reference, and working electrodes, respectively.

4.3. Transient absorption measurements

The transient absorption spectra were measured by the pump and probe method using a regeneratively amplified titanium sapphire laser (Spectra-Physics, Spitfire Pro F, 1 kHz) pumped by a Nd:YLF laser (Spectra-Physics, Empower 15). The seed pulse was generated by a titanium sapphire laser (Spectra-Physics, Mai Tai VFSJW; fwhm 80 fs). The second harmonic generation of the fundamental light (400 nm, 3 μJ pulse⁻¹) or the output of the optical parametric amplifier (780 nm, 5 μJ pulse⁻¹, Spectra-Physics, OPA-800CF-1) was used as the excitation pulse. A white light continuum pulse, which was generated by focusing the residual of the fundamental light on a sapphire crystal after the computer controlled optical delay, was divided into two parts and used as the probe and the reference lights, of which the latter was used to compensate the

laser fluctuation. The samples were sealed in a cuvette with rotating that the absorptions of the NMP dispersion at 400 nm or 780 nm were adjusted to ~1.3 OD by using 2 mm path length of quartz cuvette. The pump pulse was chopped by the mechanical chopper synchronized to one-half of the laser repetition rate, resulting in a pair of spectra with and without the pump, from which the absorption change induced by the pump pulse was estimated. All measurements were carried out at room temperature.

4.4. Photocatalytic H₂ evolution

1 mL BP aqueous dispersion (0.2 mg mL⁻¹), 200 μL EDTA solution (0.5 M) and 1 mL Pt/RGO dispersion (RGO and Pt, 0.1 mg and 75 μg, respectively) mixed with 3.8 mL water added into a 35 mL cylinder reactor and sealed with a rubber septum. The system was deaerated by Ar bubbling into the solution for 30 min before the reaction. The solution was stirred continuously and irradiated by a Xenon lamp (Asahi Spectra, HAL-320W, output wavelength: 350–1800 nm) at room temperature. The gases produced were analyzed with a gas chromatograph (Shimadzu GC-8A) equipped with an MS-5A column and a thermal conductivity detector (TCD). For visible and NIR light photocatalytic H₂ evolution, 420 nm and 780 nm long pass filter were put before the reactor, respectively. For 808 nm laser NIR light photocatalytic H₂ evolution, a 2 W 808 nm portable infrared laser (Highlasers, HK) was used as light source.

The AQEs were measured at various monochromatic lights which were obtained by using a series of band-pass filters. The AQE was calculated as follow:

$$AQE = \frac{N_e}{N_p} \times 100\% = \frac{2 \times n_{H_2} \times N_A \times h \times c}{S \times P \times t \times \lambda} \times 100\%$$

where, N_p is the total incident photons, N_e is the total reactive electrons, n_{H_2} is the amount of H₂ molecules, N_A is Avogadro constant, h is the Planck constant, c is the speed of light, S is the irradiation area, P is the intensity of irradiation light, t is the photoreaction time and λ is the wavelength of the monochromatic light.

The transmissions spectra and corresponding light intensities of the different long pass filters and band pass filters were summarized in Fig. S23 and Table S2. For AQE experiments, 1 mL BP aqueous dispersion (1 mg mL⁻¹), 200 μL EDTA solution (0.5 M) and 1 mL Pt/RGO dispersion (RGO and Pt, 0.5 mg and 0.38 mg, respectively) mixed with 3.8 mL water were used.

Acknowledgment

This work has been partly supported Grant-in-Aid for Scientific Research (project 25220806 and others) from the Ministry of Education, Culture, Sports, Science and Technology of the Japanese Government. M.Z. thanks the JSPS for a Postdoctoral Fellowship for Foreign Researchers (NO. P15346).

Appendix A. Supplementary data

Supplementary data associated with this article can be found, in the online version, at <http://dx.doi.org/10.1016/j.apcatb.2017.06.002>.

References

- [1] M.S. Dresselhaus, I.L. Thomas, *Nature* 414 (2001) 332–337.
- [2] T.P. Yoon, M.A. Ischay, J. Du, *Nat. Chem.* 2 (2010) 527–532.
- [3] Y. Tachibana, L. Vayssières, J.R. Durrant, *Nat. Photonics* 6 (2012) 511–518.
- [4] T. Hisatomi, J. Kubota, K. Domen, *Chem. Soc. Rev.* 42 (2014) 7520–7535.
- [5] X.B. Chen, S.H. Shen, L.J. Guo, S.S. Mao, *Chem. Rev.* 110 (2010) 6503–6570.
- [6] A.A. Ismail, D.W. Bahneemann, *Sol. Energy Mater. Sol. C* 128 (2014) 85–101.
- [7] A. Fujishima, K. Honda, *Nature* 238 (1972) 37–38.
- [8] B. Qiu, Q. Zhu, M. Du, L. Fan, M. Xing, J. Zhang, *Angew. Chem. Int. Ed.* 56 (2017) 2684–2688.
- [9] J. Tian, Y.H. Sang, G.W. Yu, H.D. Jiang, X.N. Mu, H. Liu, *Adv. Mater.* 25 (2013) 5075–5080.
- [10] W.Q. Zou, C. Visser, J.A. Maduro, M.S. Pshenichnikov, J.C. Hummelen, *Nat. Photonics* 6 (2012) 560–564.
- [11] X.H. Zhang, L.J. Yu, C.S. Zhuang, T.Y. Peng, R.J. Li, X.G. Li, *ACS Catal.* 4 (2014) 162–170.
- [12] X.Y. Wu, S. Yin, Q. Dong, B. Liu, Y.H. Wang, T. Sekino, S.W. Lee, T. Sato, *Sci. Rep.* 3 (2013) 2918.
- [13] X. Zhang, H. Huang, J. Liu, Y. Liu, Z.H. Kang, *J. Mater. Chem. A* 1 (2013) 11529–11533.
- [14] G. Wang, B.B. Huang, X.C. Ma, Z.Y. Wang, X.Y. Qin, X.Y. Zhang, Y. Dai, M.H. Whangbo, *Angew. Chem. Int. Ed.* 52 (2013) 4810–4813.
- [15] L.K. Li, Y.J. Yu, G.J. Ye, Q.Q. Ge, X.D. Ou, H. Wu, D.L. Feng, X.H. Chen, Y.B. Zhang, *Nat. Nanotechnol.* 9 (2014) 372–377.
- [16] H. Liu, Y.C. Du, Y.X. Deng, P.D. Ye, *Chem. Soc. Rev.* 44 (2015) 2732–2743.
- [17] L.Z. Kou, C.F. Chen, S.C. Smith, *J. Phys. Chem. Lett.* 6 (2015) 2794–2805.
- [18] A. Castellanos-Gomez, *J. Phys. Chem. Lett.* 6 (2015) 4280–4291.
- [19] F.N. Xia, H. Wang, Y.C. Jia, *Nat. Commun.* 5 (2014) 4458.
- [20] D. Hanlon, C. Backes, E. Doherty, C.S. Cucinotta, N.C. Berner, C. Boland, K. Lee, A. Harvey, P. Lynch, Z. Gholamvand, S.F. Zhang, K.P. Wang, G. Moynihan, A. Pokle, Q.M. Ramasse, N. McEvoy, W.J. Blau, J. Wang, G. Abellán, F. Hauke, A. Hirsch, S. Sanvito, D.D. O'Regan, G.S. Duesberg, V. Nicolosi, J.N. Coleman, *Nat. Commun.* 6 (2015) 8563.
- [21] H.T. Yuan, X.G. Liu, F. Afshinmanesh, W. Li, G. Xu, J. Sun, B. Lian, A.G. Curto, G.J. Ye, Y. Hikita, Z.X. Shen, S.C. Zhang, X.H. Chen, M. Brongersma, H.Y. Hwang, Y. Cui, *Nat. Nanotechnol.* 10 (2015) 707–714.
- [22] M. Buscema, D.J. Groenendijk, G.A. Steele, H.S.J. Zant, A. Castellanos-Gomez, *Nat. Commun.* 5 (2014) 4651.
- [23] M. Buscema, D.J. Groenendijk, S.I. Blanter, G.A. Steel, H.S. Zant, A. Castellanos-Gomez, *Nano Lett.* 14 (2014) 3347–3352.
- [24] S.B. Lu, L.L. Miao, Z.N. Guo, X. Qi, C.J. Zhao, H. Zhang, S.C. Wen, D.Y. Tang, D.Y. Fan, *Opt. Express* 23 (2015) 11183–11194.
- [25] H. Wang, X.Z. Yang, W. Shao, S.C. Chen, J.F. Xie, X.D. Zhang, J. Wang, Y. Xie, J. Am. Chem. Soc. 137 (2015) 11376–11382.
- [26] B.S. Sa, Y. Li, J.S. Qi, R. Ahuja, Z.M. Sun, *J. Phys. Chem. C* 118 (2014) 26560–26568.
- [27] M.Z. Rahman, C.W. Kwong, K. Davey, S.Z. Qiao, *Energy Environ. Sci.* 9 (2016) 709–728.
- [28] J. Hu, Z.K. Guo, P.E. Mcwilliams, J.E. Darges, D.L. Druffel, A.M. Moran, S.C. Warren, *Nano Lett.* 16 (2016) 74–79.
- [29] Z.R. Shen, S.T. Sun, W.J. Wang, J.W. Liu, Z.F. Liu, J.C. Yu, *J. Mater. Chem. A* 3 (2015) 3285–3288.
- [30] W. Lei, T. Zhang, P. Liu, J.A. Rodriguez, G. Liu, M. Liu, *ACS Catal.* 6 (2016) 8009.
- [31] M.S. Zhu, X. Cai, M. Fujitsuka, J. Zhang, T. Majima, *Angew. Chem. Int. Ed.* 56 (2017) 2064–2068.
- [32] Z.N. Guo, H. Zhang, S.B. Lu, Z.T. Wang, S.Y. Tang, J.D. Shao, Z.B. Sun, H.H. Xie, H.Y. Wang, X.F. Yu, P.K. Chu, *Adv. Funct. Mater.* 25 (2015) 6996–7002.
- [33] C. Hao, F. Wen, J. Xiang, S. Yuan, B. Yang, L. Li, W. Wang, Z. Zeng, L. Wang, Z. Liu, Y. Tianal, *Adv. Funct. Mater.* 26 (2016) 2016–2024.
- [34] Y. Amao, *ChemCatChem* 3 (2011) 458–474.
- [35] S. Fukuzumi, Y.J. Yamada, *Mater. Chem.* 22 (2012) 24284–24296.
- [36] A. Iwase, Y.H. Ng, Y. Ishiguro, A. Kudo, R. Amal, *J. Am. Chem. Soc.* 133 (2011) 11054–11057.
- [37] B. Qiu, Q. Li, B. Shen, M. Xing, J. Zhang, *Appl. Catal. B: Environ.* 183 (2016) 216–223.
- [38] G.G. Liu, T. Wang, H.B. Zhang, X.G. Meng, D. Hao, K. Chang, P. Li, T. Kako, J.H. Ye, *Angew. Chem. Int. Ed.* 54 (2015) 13561–13565.
- [39] M.S. Zhu, C.Y. Zhai, M.J. Sun, J.Y. Hu, B. Yan, Y.K. Du, *Appl. Catal. B: Environ.* 203 (2017) 108–115.
- [40] C. Zhai, M. Zhu, F. Pang, D. Bin, C. Lu, M.C. Goh, P. Yang, Y. Du, *ACS Appl. Mater. Interfaces* 8 (2016) 5972–5980.
- [41] X.G. Li, W.T. Bi, L. Zhang, S. Tao, W.S. Chu, Q. Zhang, Y. Luo, C.Z. Wu, Y. Xie, *Adv. Mater.* 28 (2016) 2427–2431.
- [42] A. Furube, T. Asahi, H. Masuhara, H. Yamashita, M. Anpo, *Chem. Phys. Lett.* 336 (2001) 424–430.
- [43] B.C. Fitzmorris, G.K. Larsen, D.A. Wheeler, Y. Zhao, J.Z. Zhang, *J. Phys. Chem. C* 116 (2012) 5033–5041.
- [44] P. Yu, X. Wen, Y. Lee, W. Lee, C. Kang, J. Tang, *J. Phys. Chem. Lett.* 4 (2013) 3596–3601.
- [45] E.-C. Su, *ACS Sustainable Chem. Eng.* 5 (2017) 2146–2153.
- [46] H.D. Mansilla, C. Bravo, R. Ferreyra, M.I. Litter, W.F. Jardim, C. Lizama, J. Freer, J. Fernández, *J. Photochem. Photobiol. A: Chem.* 181 (2006) 188–194.
- [47] B.B. Yang, J. Wang, D. Bin, M.S. Zhu, P. Yang, Y.K. Du, *J. Mater. Chem. B* 3 (2015) 7440–7448.